Biomaterials Science

ROYAL SOCIETY OF CHEMISTRY

PAPER

View Article Online
View Journal | View Issue

Cite this: *Biomater. Sci.*, 2024, **12**, 1549

Assessing the influence of small structural modifications in simple DNA-based nanostructures on their role as drug nanocarriers†

Alejandro Postigo, [a] Pablo Martínez-Vicente, [a] Kevin N. Baumann, [b] Jesús del Barrio [a] and Silvia Hernández-Ainsa *[a,c]

Received 5th December 2023,
Accepted 16th January 2024

DOI: 10.1039/d3bm01987j

rsc.li/biomaterials-science

DNA nanotechnology leverages Watson–Crick–Franklin base-pairing interactions to build complex DNA-based nanostructures (DNS). Due to DNA specific self-assembly properties, DNS can be designed with a total control of their architecture, which has been demonstrated to have an impact on the overall DNS features. Indeed, structural properties such as the shape, size and flexibility of DNS can influence their biostability as well as their ability to internalise into cells. We present here two series of simple DNS with small and precise variations related to their length or flexibility and study the influence that these structural changes have on their overall properties as drug nanocarriers. Results indicate that shorter and more flexible DNS present higher stability towards nuclease degradation. These structural changes also have a certain effect on their cell internalisation ability and drug release rate. Consequently, drug-loaded DNS cytotoxicity varies according to the design, with lower cell viability values obtained in the DNS exhibiting faster drug release and larger cell interaction rates. In summary, small changes in the structure of simple DNS can have an influence on their overall capabilities as drug nanocarriers. The effects reported here could guide the design of simple DNS for future therapeutic uses.

1. Introduction

DNA nanotechnology enables the development of nanostructures with total control over their size and shape in a reproducible way. This ability is based on the fundamental properties of DNA, in particular the highly specific base pair recognition and thus programmable self-assembly.[1–3] These DNA nanostructures (DNS) have additional advantages of good biocompatibility, water solubility as well as easy and controllable functionalisation. Hence, DNS have been suggested as promising candidates for several applications in biomedicine, especially as nanocarriers for therapeutic agents in different modalities, such as chemotherapy and gene therapy.[2,4,5] DNA nanostructures have been reported to show low immunogenic response, but they can be adapted with appropriate sequences and decorated with antigens to elicit immune response and hence display interesting applications for immunotherapy.[6–8] Indeed, there is a large variety of DNS developed to this end spanning from simpler designs, such as a Y-shaped motif or a DNA tetrahedron,[9] to more complex constructs based on DNA origami.[10,11] Understanding the effect of certain structural features on several crucial properties such as stability and cell internalisation ability is important to guide DNS design and hence facilitate their applicability.[11] Some research has been carried out in this direction,[8,12–14] mostly focused on complex DNA origami-based structures.[8,12,14] Specifically, larger and compact DNA origami structures were reported to exhibit better cellular uptake than elongated ones.[12]

However, considering future clinical applicability, less complex DNS than origami could entail advantages such as reduced material costs and simplicity of production. Thus, investigating the structure-dependent properties of simpler DNS designs may benefit future translation. For instance, the effect of the topology of different 3D DNA polyhedra on their uptake *in vitro* and *in vivo* has been recently described. Among several explored polyhedral designs, the DNA tetrahedron showed better uptake in several cell lines as well as *in vivo*.[13] Here, we focus our investigation on two series of simple DNS that exhibit a straightforward design and are easy to produce and scalable. In particular, we have prepared a set of DNS using the single-stranded tile (SST) approach[15] that presents differences in their length (Fig. 1a) and another set of Y-shaped DNS built by the assembly of 3 oligonucleotides with differences related to their flexibility (Fig. 1b). For each series, we have studied the effect that subtle changes in these struc-

[a]*Instituto de Nanociencia y Materiales de Aragón, CSIC–Universidad de Zaragoza, Zaragoza 50009, Spain. E-mail: silviamh83@unizar.es*
[b]*Biozentrum, University of Basel, 4056 Basel, Switzerland*
[c]*ARAID Foundation, Government of Aragon, Zaragoza 50018, Spain*
† Electronic supplementary information (ESI) available. See DOI: https://doi.org/10.1039/d3bm01987j

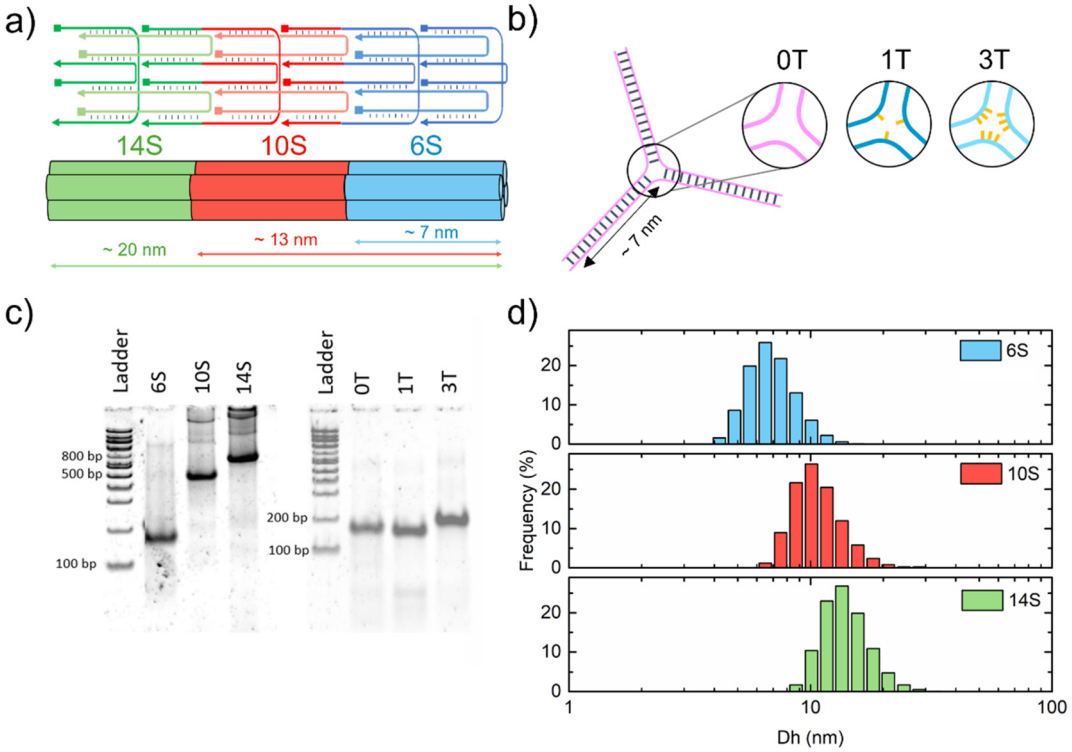

Fig. 1 DNS design and structural characterisation. (a) SST series design layout. Number of strands correlating with length, with 6S, 10S and 14S being composed of 6, 10 and 14 strands, respectively. (b) Y-shaped DNSs (0T, 1T and 3T), with either 0, 1 or 3 unpaired thymines at the hinge, indicated in yellow. (c) PAGE analysis of different DNSs. A a 100 bp ladder is included in the first lane. (d) Histograms of the hydrodynamic diameter (D_h) values (in number) obtained by DLSs for the SST DNS series (n = 10).

tural features, namely length and flexibility, have on their stability towards nuclease degradation and in cell culture media, their internalisation by cells, their drug loading and release capacity, and their effect on cell viability. Our work will benefit the research community focused on the design of simple DNS for therapeutic delivery purposes.

2. Results and discussion

2.1. Assembly and characterisation of DNS

Two series of DNS were synthesised, called SST and Y-shaped. The SST series is constituted by three assembled DNS which comprise six, ten or fourteen strands (named 6S, 10S and 14S, respectively) into a 4-helix bundle with a rectangular prism cross-section using the SST assembly method (Fig. 1a).[15–17] This series was used to study the effect of small variations in the length, while maintaining the height and width of the cross-sectional area constant (effectively increasing the aspect ratio; Fig. 1a), on the aforementioned biological properties. In this series, the negative charge of the DNS also increases with the length, although the change in the charge/mass ratio is negligible. The Y-shaped series is formed by three Y-shaped DNS assembled with three strands. These DNS differ in the number of unpaired thymine (T) bases present at the hinge (zero, one or three) and are named 0T, 1T and 3T, respectively. The introduction of unpaired bases at the hinge of Y-shaped DNS has been reported to modify conformational flexibility.[18,19] Thus, this Y-shaped series was designed to study the effect of variations of the flexibility, with the 3T DNS presenting the largest flexibility of the hinge (Fig. 1b).[20] Both series were assembled using thermal annealing protocols adapted from previous reports (see the Experimental section for further details and Table S1 in the ESI† for oligonucleotide sequences). The correct folding of the DNS was initially assessed by polyacrylamide gel electrophoresis (PAGE) (Fig. 1c). The formation of one predominant band for every structure verifies the correct assembly of both SST and Y-shaped series. Concerning SST DNS, distinct bands for each DNS can be observed, with 10S running slower than 6S and faster than 14S due to the larger molecular weight and size. Note that some lower intensity bands with lower mobility are observed in 10S and 14S which could be related to the presence of some multimers. Regarding the Y-shaped DNS, it is remarkable that 0T presents slightly lower mobility in the gel than 1T, even though it does contain a small number of nucleotides, which supports its larger rigidity.[18,20] A dynamic light scattering (DLS) study was also performed to corroborate the right formation of DNS and their differences in size (Fig. 1d and Fig. S2†). Namely, a hydrodynamic diameter (D_h) of 7.1 ± 1.6 nm, 10.9 ± 0.4 nm and 14.2 ± 1.6 nm were obtained for 6S, 10S and 14S, respectively (Table S2†). As expected, the

longer the DNS, the larger the experimentally obtained D_h value. Similar D_h values were obtained for the DNS in the Y-shaped series (6.8 ± 1.1 nm for 0T, 6.5 ± 1.1 nm for 1T and 7.2 ± 1.9 nm for 3T; see Table S2†). Regarding thermal stability, all DNS show melting temperatures (T_m) above 37 °C (all recorded at the same DNA concentration, *i.e.* 20 ng μL^{-1}), with T_m values of around 40 °C for SST and around 70 °C for the Y-shaped DNS (see Fig. S3 and Table S3†). D_h and T_m values are similar for the DNS both in PBS and in a solution containing 50% of cell culture DMEM (see Tables S2 and S3†), thus supporting their structural and thermal stability under cell culture conditions.

2.2. Stability in nuclease-containing solutions

One important aspect concerning the use of DNS as drug nanocarriers is assessing their stability in solutions that contain nucleases to mimic biological environments. Even though biodegradation is a desired property for these nanomaterials, DNS should present certain biostability to fulfil their biological function. To study the effect that the subtle proposed changes in our DNS have on the stability against nuclease degradation, both SST and Y-shaped DNS were incubated at 37 °C with either the cell culture DMEM supplemented with fetal bovine serum (FBS) (Fig. 2a and c) or with DNase I (Fig. 2b and d), see also Fig. S4 in the ESI.† After several incubation time intervals, the DNS stability was assessed using PAGE. In the case of the SST series, the shortest structure, 6S is observed to present the slowest degradation rate when incubated with DMEM + FBS (Fig. 2a), suggesting that shorter length in this type of design is preferred to confer higher resistance to serum containing solutions. No differences are observed though when SST DNS are incubated with DNase I (Fig. 2b), suggesting that differences in the serum stability do not arise from this type of nuclease. With respect to the Y-shaped series, the 3T design presents the highest resistance in serum (Fig. 2c) and DNase I (Fig. 2d), followed by 1T with 0T as the less stable DNS. This suggests that higher flexibility at the hinge of the Y-shaped DNS is related to less nuclease susceptibility. The different number of unpaired nucleotides at the hinge modifies the flexibility and the chemical environment of the junction of these DNS, which have been reported to affect DNAse I activity.[21,22] Therefore, these small design changes that modify the length and flexibility appear as a facile approach for tuning the vulnerability of DNS in nuclease-containing solutions. Additionally, when comparing both DNS series, the differences are remarkable in both serum and DNase I solutions. Regarding serum, no degradation was observed in the Y-shaped DNS even after 7 days of incubation with 10% FBS (see Fig. S4c in the ESI†) and differences were observed with FBS at 50% (Fig. 2c), but the SST series do show degradation at 10% FBS in 24 h (Fig. 2a). Similarly, in the case of DNase I, larger concentrations were required to observe degradation in the Y-shaped series compared to the SST series (Fig. 2b and d). Thus, Y-shaped DNS were found to be more resistant against nuclease degradation than SST, which suggests that these simpler designs confer higher stability in biologically relevant media. It is important to remark that PAGE was also performed with DNS in PBS incubated at 37 °C for up to 24 h and that all DNS remain structurally stable (see Fig. S4a and c in the ESI†). Therefore, the changes observed by PAGE are caused by nuclease-mediated digestion and not by thermal disassembly. We also probed that DNS are stable under slightly acid or basic conditions (see Fig. S5†).

2.3. Cell internalisation

DNS acting as nanocarriers of therapeutic agents should be internalised by cancer cells. DNS are commonly internalised

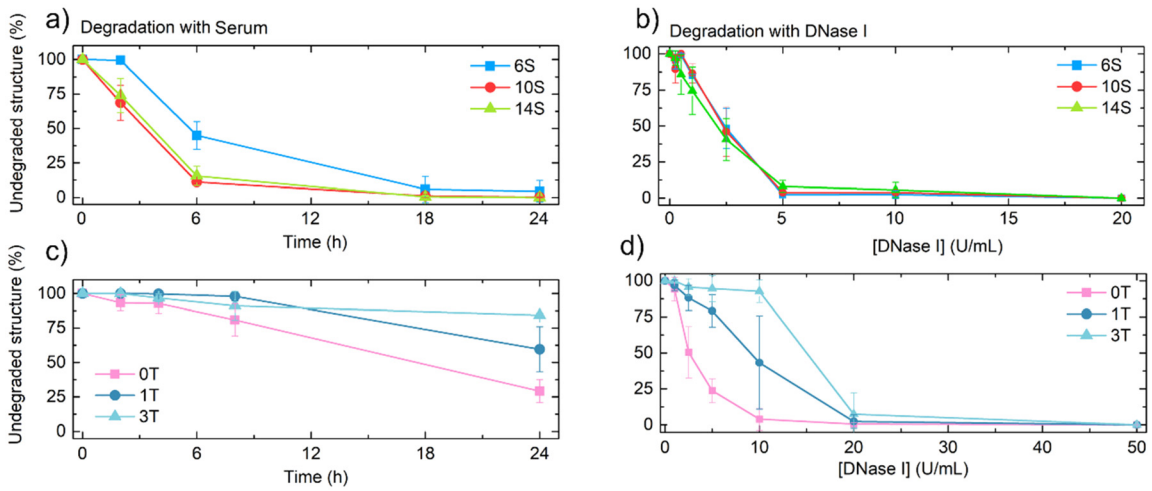

Fig. 2 Nuclease resistance study. (a) and (b) Remaining 6S (blue data), 10S (red data) and 14S (green data) estimated by PAGE analysis after incubation with (a) DMEM containing 10% FBS at 37 °C at different time points or (b) at 37 °C during 1 h with different concentrations of DNase I. (c) and (d) Remaining 0T (pink data), 1T (dark blue data) and 3T (light blue data) after incubation with (c) DMEM containing 50% FBS at 37 °C at different time points or (d) after 1 h of incubation at 37 °C with different concentrations of DNase I.

by endocytic vesicles following receptor-mediated endocytosis.[11,23–25] The potential impact of the structural changes on the cell internalisation ability was also investigated for the two series of DNS by flow cytometry and confocal microscopy. To this end, DNS were folded with one Atto488 fluorescently labelled oligonucleotide (see Table S1 in the ESI†). Additionally, the cells were incubated with a single Atto488 labelled strand (S). Flow cytometry analysis was performed for two types of cancer cell lines: MIA PaCa-2 (Fig. 3a, b and Fig. S6a, c†) and HeLa (Fig. S6b, d†) incubated with the different DNS for 3 hours. In both cases, histograms of the geometric mean fluorescence intensity (gMFI) show the total amount of cells with the fluorescence signal (Fig. S6†) showing the ability of DNS to interact with cancer cells. To compare results and to determine structure-dependent cell interactions, gMFI data are normalised by S. Fig. 3 shows the normalised gMFI values of MIA PaCa-2 cells incubated with the different DNS. No significant differences between DNS can be observed in the case of the SST series (Fig. 3a). Nonetheless, lower normalised gMFI values of DNS are observed in cells when compared with those incubated with S. On the other hand, significant differences between DNS can be observed in the case of the Y-shaped series in MIA PaCa-2 cells (Fig. 3b) where less flexible 0T and 1T display larger intensity and hence better interaction than 3T. These results show that these structural changes in simple DNS influence their ability to interact with cells. Regarding the comparison with S, 0T and 1T DNS show higher mean fluorescence than the S control. In the case of HeLa cells, no significant differences were observed in the gMFI values caused by DNS (Fig. S6†), which evidences that the uptake efficiency of DNS can vary depending on the cell type, as reported before.[5,12,14,26] To obtain information about the actual cellular uptake ability and following previous reports,[27] flow cytometry analysis was also performed in cells after their incubation with DNS and subsequent treatment with high amount of DNase I, with the aim to degrade any DNS attached to the membrane (see Fig. S7†). Similar intensity values are obtained for DNase I treated or untreated cells, thus corroborating cell fluorescence accounts for actual cellular uptake of the DNS.

Furthermore, confocal microscopy was carried out with the MIA PaCa-2 cell line to confirm the internalisation ability of the DNS into the cancer cells (Fig. 4 and Fig. S8†). As an example, images were obtained for MIA PaCa-2 incubated for 3 h with either 14S (Fig. 4a and b) or 1T (Fig. 4c and d). First, orthogonal projection of specific confocal images (Fig. 4a and c) demonstrates the accumulation of several DNS inside cells. Additionally, the maximum intensity projection shows the DNS that can be observed at the same confocal plane as the cell nucleus (see white arrows in Fig. 4b and d).

2.4. Drug cargo encapsulation and release

Doxorubicin (DOX), a widely used anticancer drug, was used as a cargo model. DOX anticancer action resides in its ability to intercalate into double-stranded (dsDNA) DNA and, hence, stop replication and transcription processes.[28] Since DOX fluorescence is reduced upon intercalation into dsDNA, its loading into DNS can be tracked with fluorescence measurements.[29,30] These two properties make DOX a common candidate for the validation of DNS as drug nanocarriers.[29,31–34] In our study, a constant concentration of DOX (10 μM) was titrated while varying the DNS concentration (see Fig. S9† for an example of titration with 0T). Precisely, the number of base pairs (bp) required to trap one DOX molecule was calculated obtaining a

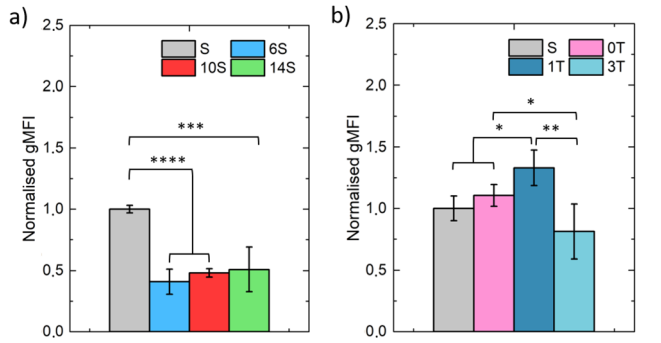

Fig. 3 Flow cytometry analysis of MIA-PaCa-2 cells incubated with (a) SST DNS or (b) Y-shaped DNS previously labelled with Atto488. Bar graphs show geometric mean fluorescence intensity (gMFI) values normalized by the S. gMFI data are the averaged values and the standard deviation ($n \geq 3$) of two independent studies. *P*-values were calculated using the *t*-test analysis, $*P < 0.05$, $**P < 0.01$, $***P < 0.001$, $****P < 0.0001$.

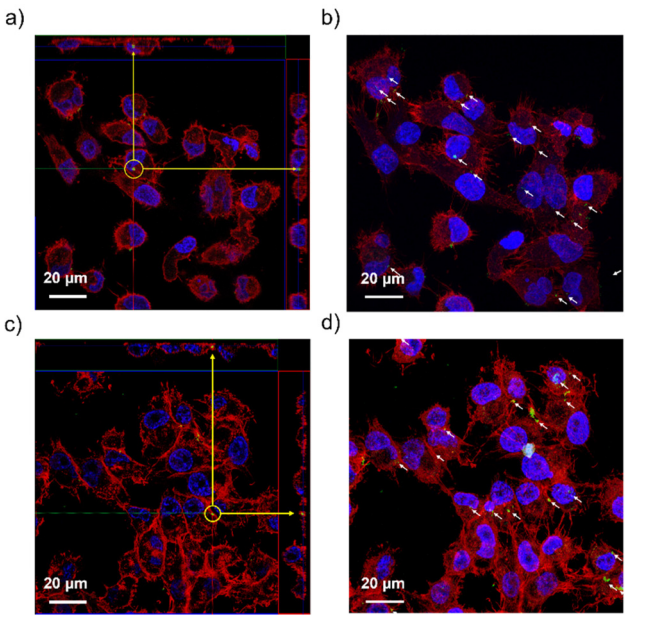

Fig. 4 Confocal laser scanning microscopy images of MIA-PaCa-2 cells incubated with 6S (a and b) or 1T (c and d). In (a) and (c) an orthogonal projection of the marked plane is observed at the right and top part of images. In (b) and (d) maximum intensity projections of all z images which correlate with the plane of the cell nucleus. Nuclei can be seen in blue (DAPI-staining), actin in red (phalloidin-AlexaFluor546 staining) and DNS in green (Atto488-labelled). Scale bar is 20 μm.

value in the range of 3.7 to 4.5 bp/DOX for all DNS. (Table S4†). To further characterise this trapping efficiency, isothermal calorimetry (ITC) was performed in 0T and 6S as an example (Fig. S10†). bp/DOX values of 4.4 and 4.5 were obtained by ITC. These values are consistent with fluorescence measurements, and both demonstrate the ability of DNS to trap DOX and provide the amount of drug present as cargo.

DOX release was also investigated by fluorescence measurements (Fig. 5). While DNS degradation occurs, released DOX produces an increase in sample fluorescence. Aiming at mimicking biological conditions, the DOX release profile over time was investigated by incubating the DNS with both DMEM supplemented with FBS and with DNase I at 37 °C. Regarding the SST series, the DOX release reaches maximum values after 24 h of incubation in DMEM + FBS 10% (Fig. 5a), with a similar release rate for all DNS. Conversely, when incubated with DNase I, differences between DNS can be observed. Namely, 6S shows a lower DOX release rate, of around 62 ± 3% within 20 U mL^{-1}, whereas 10S and 14S show 78 ± 1 and 76 ± 2% in 20 U mL^{-1} DNase I, respectively (Fig. 5b). As for Y-shaped DNS, differences between the structures can be observed in both DMEM + 10% FBS and DNase I (Fig. 5c and d). 0T shows the highest release rate, reaching 75 ± 10% of DOX release after 24 h of incubation in DMEM + FBS and 100% when incubated with 50 U mL^{-1} DNase I. These results are in agreement with the stability data reported in the previous section (Fig. 2) with 0T, 10S and 14S showing enhanced structural vulnerability in nuclease-containing solutions.

2.5. Cell viability of DOX-loaded DNS

Finally, we investigated the effect on cell viability produced by the DNS of the two series loaded with DOX. In particular, a tetrazolium dye (MTT) viability assay in cells incubated with DOX for 3 hours either free or loaded in the DNS at two different DOX concentrations but keeping the DNA/DOX ratio constant (5 bp/DOX). Assays were performed in two different cancer cell lines (MIA PaCa-2 and HeLa). The results are shown in Fig. 6 and Fig. S11.† In the case of MIA PaCa-2 cells some differences in cell viability can be observed for both DNS series. In the SST series (Fig. 6a), shorter 6S DNS display the largest cell viability value with no significant differences found between 10S and 14S. In the case of Y-shaped DNS (Fig. 6b), 3T shows a larger cell viability value, with 0T reducing the cellular viability to a larger extent than the rest of the series. These observed differences in cell viability connect to a certain extent with their ability to interact with cells (Fig. 3) as well as their stability in serum-containing solutions (Fig. 2) and DOX release rate (Fig. 5). Regarding the Y-shaped series, 3T is the DNS showing the lowest cell internalisation ability (Fig. 3b), the largest stability in serum (Fig. 2c) within the series and, together with 1T, the slowest DOX release rate (Fig. 5d). This can relate to the lower effect of DOX-loaded 3T on the cell via-

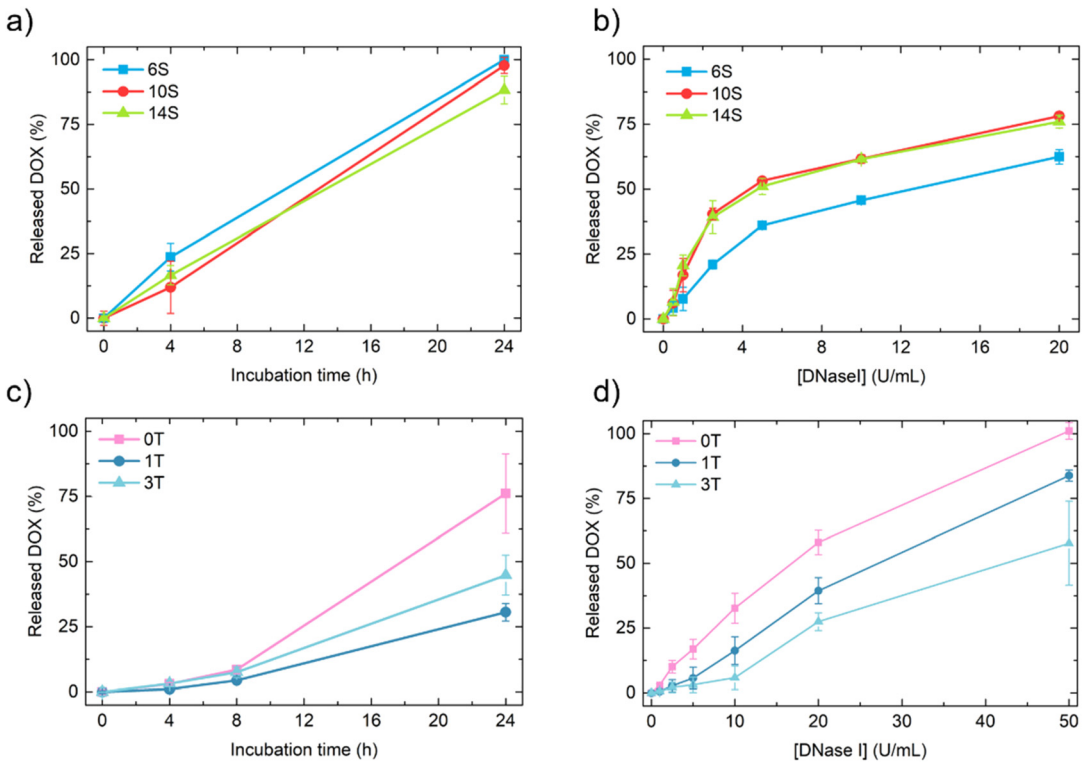

Fig. 5 DOX release studies. (a) and (b) Release profile of DOX loaded in 6S (blue data), 10S (red data) and 14S (green data) after incubation at 37 °C with (a) DMEM containing 10% FBS at different time points or (b) during 1 h with different concentrations of DNase I. (c) and (d) Release profile of DOX loaded in 0T (pink data), 1T (dark blue data) and 3T (light blue data) after incubation at 37 °C with (c) DMEM containing 10% FBS at different time points or (d) during 1 h with different concentrations of DNase I.

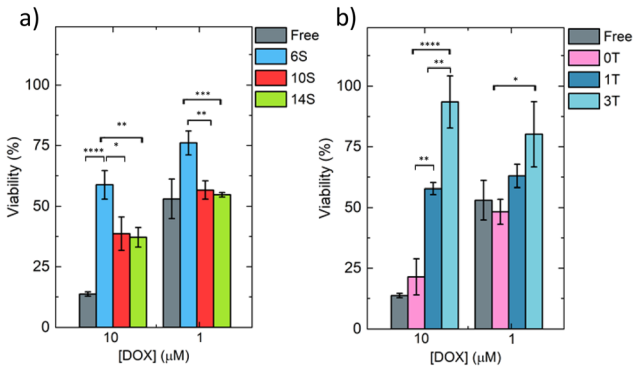

Fig. 6 MIA PaCa-2 cell viability analysis using the MTT assay for DOX encapsulated in DNS after 3 h of incubation with cells, followed by a washing step to eliminate DOX not interacting with cells, and a subsequent 24 hour incubation. (a) SST and (b) Y-shaped. Data are the averaged values (n = 3) with associated standard P-values calculated using one-way ANOVA, *P < 0.05, **P < 0.01, ***P < 0.001, ****P < 0.0001 comparing every group with each other.

bility (Fig. 6b). In contrast, 0T shows larger cell internalisation (Fig. 3b), presents the largest structural vulnerability (Fig. 2c) and the quickest DOX release profile (Fig. 5d), which connects well with their larger impact on reducing cellular viability (Fig. 6b). Regarding the SST DNS series, 6S is the structure displaying the lowest influence on cell viability (Fig. 6a). In this series, no significant differences were observed in their cell internalisation, so the enhanced cell viability by 6S may be associated with its larger stability (Fig. 2a) and a slower DOX release profile (Fig. 5b). It is worth noting that cell viability values exhibited by free DOX are lower than the DOX-loaded DNS, which may be related to a weak internalisation ability of DNS during the 3 hours of incubation of these studies or on more complex release processes of DOX inside the cells. In the case of HeLa cells, similar differences were observed in the SST series at 10 μM DOX, with 6S showing the largest cell viability (Fig. S11†). Nevertheless, no further differences were observed. This variability in cell viability by DNS as a function of the cell type may be based on the cell-type influence on DNS cell internalisation capabilities (see section 2.3)[12,14,26] and highlights the importance of adequately selecting the DNS structure for a particular cell line.

3. Conclusions

In this work, we have studied the effect that small changes in the structure of simple DNS related to their length and flexibility have on their properties as drug nanocarriers. DNS have shown different stabilities towards nuclease degradation with the shorter (6S) in the SST series and more flexible (3T) in the Y-shaped series exhibiting the largest structural stability in nuclease-containing solutions. Some differences are observed in the ability of the Y-shaped series to be internalised by MiaPaCa-2 cells, but no effect was observed in HeLa cells. DNS of the SST series do not show any difference in their ability to be internalised by either of the investigated cell lines. The DOX release rate is indeed dependent on structural changes and correlates well with the resistance to nuclease degradation in the case of the Y-shaped DNS series. Concerning cell viability, DOX-loaded DNS present different cytotoxicity effects in MIA PaCa-2 cells, with the results related to the internalisation ability, nuclease-mediated degradation and DOX release. However, almost no significant differences in cytotoxicity are observed in DOX-loaded DNS in HeLa cells, indicating the importance of the type of cell in the design of a particular nanostructure as a drug carrier. Although there is a lack of standardized reported results in the DNA nanotechnology field,[35,36] we can conclude that, overall, our simple design DNS show outstanding properties regarding stability in free-Mg^{2+} physiological buffers and resistance against serum degradation compared to complex DNA origamis. For instance, a reported icosahedral origami does show a high amount of degradation after 6 h incubation in FBS-containing media.[37] Other no origami-based DNS, like the tetrahedron DNS, do show stability for up to 23 h.[38] However, especially relevant is the large stability exhibited by the Y-shaped DNS series reported here, which remain structurally stable even after a week of incubation with 10% FBS containing DMEM. Besides, regarding cellular internalization, our results are in accordance with those reported for other DNS when using ssDNA as the control.[27,39] Concerning DOX trapping, we observe similar DOX loading properties in all DNS with no significant influence of the DNS structure as described before.[29] Furthermore, our results reveal how small changes in the structure of simple DNS can have an influence on their overall capabilities as drug nanocarriers, without compromising DNA-based nanostructure properties, as it happens with other modification strategies.[40] A key aspect of our DNS is that they are easy to design and prepare. Additionally, their fabrication cost is lower compared to origami-based ones, which points them as better candidates for potential industrial production.[41]

The effects reported here could guide the design for future therapeutic uses. The uptake of non-decorated DNS has been investigated here to explore the impact of the structure itself on the ability to be internalised. To achieve selectivity and enhance the efficiency of uptake, precise decoration with targeting moieties such as aptamers or antibodies could be integrated.[42–44] Also, the decrease in DOX cytotoxicity by encapsulation into DNS could be exploited in the future, upon adequate surface ligand decoration, to selectively enhance the therapeutic effect in target cells while diminishing the off-target cytotoxicity of DOX. Furthermore, differences associated with the small structural changes in both series could be adapted for the delivery of combined therapies with different pharmacokinetic profiles.

4. Materials and methods

4.1. DNS fabrication

Oligonucleotides were purchased from IDT or Macrogen. Atto488-labelled oligos were obtained from Biomers.

Oligonucleotides were stored in nuclease-free water at −20 °C. 6S, 0T, 1T and 3T were assembled at equimolar concentrations in 1× phosphate buffered saline (PBS) (pH = 7.4) solution. 10S and 14S were folded in a solution containing 20 mM $MgCl_2$ buffered with TE (pH = 8.2). SST DNS were assembled in a thermocycler by heating to 85 °C for 5 min, next cooling down from 85 to 65 °C in 20 steps (1 °C per step, 5 min each step) and finally cooling down from 65 to 25 °C in 80 steps (0.5 °C per step, 12 min for each step). On the other hand, Y-shaped DNS were assembled by heating at 70 °C for 30 s and cooling from 70 to 25 °C in 90 steps (0.5 °C per step, 30 s for each step). Samples were stored at 4 °C and protected from light. Once assembled, 10S and 14S were dialysed against 1× PBS with 2 kDa Slide-A-Lyzer MINI dialysis units (ThermoFisher). After dialysis, the original DNS concentration was confirmed by nanodrop measurements. See complete details in section S1 (ESI†).

4.2 DNS characterisation

The correct folding of the DNS was assessed by PAGE and DLS. For PAGE, 20–60 ng μL^{-1} DNS were loaded and run for 100 minutes at 100 V in 10% polyacrylamide gels immersed in a solution containing 11 mM $MgCl_2$ buffered with 1× TAE (pH = 8.3). As a reference, a 100 bp (New England Biolabs) ladder was run along with the samples. For subsequent visualisation, the gels were stained with GelRed (Biotium, Fremont, CA, USA) and imaged under UV light transillumination. For DLS measurements (Zeta Sizer, Malvern Instruments), DNS were folded and measured in PBS at 2 μM concentration. 10 measurements of 5 runs each were performed to obtain the average and the standard deviation of the mean (SD). Reported data are values obtained in numbers. The melting temperature (T_m) was obtained by measuring the absorbance at 260 nm of DNS at a concentration of 32 μM bp in a PBS buffer solution as a function of the temperature using a Varian CaryBio 100 UV-vis spectrophotometer. The temperature ranged from 20 °C to 95 °C with an increase of 1 °C min^{-1}. Data analysis was performed using the OriginPro 2016 software. Here, the absorbance was plotted against temperature. The derivative of the curve was calculated and fitted with a Gaussian function to provide the T_m (maximum) and the disassembling thermal range (sigma).

4.3. DNS stability in nuclease containing solutions

The structural stability of DNS against degradation by nucleases was studied with DNase I (New England Biolabs, Ipswich, USA) and with cell culture media supplemented with fetal bovine serum (FBS). SST DNS (unified to 20 ng μL^{-1}, equivalent to 400 nM for 6S, 250 nM for 10 S and 150 nM for 14S) were incubated in a solution of Dulbecco's modified Eagle's medium (DMEM) supplemented with 10% of FBS (Thermo Scientific, Waltham, MA, USA). Incubation times were set to 0, 2, 6, 18 and 24 hours. For the DNAse I study, SST DNS were incubated for 1 h in the presence of different concentrations of DNAse I: 20, 10, 5, 2.5, 1 and 0.5 units of enzyme in mL (U mL^{-1}). In the case of the Y-shaped DNS (concentration unified to 40 ng μL^{-1}, equivalent to 500 nM), DNS were incubated with DMEM supplemented with 50% FBS (due to higher nuclease resistance than the SST series) during 0, 2, 4, 8 and 24 hours. In the DNAse I study, enzyme concentrations were 50, 20, 10, 5, 2.5 and 1 U mL^{-1}. In all cases the incubation temperature was 37 °C. The stability was determined using PAGE. The mixtures were run for 100 minutes at 100 V in a 10% polyacrylamide gel using 11 mM $MgCl_2$ with 1× TAE (pH = 8.3) as the running buffer. Specifically, the degree of stability was expressed by the percentage of remaining intact structure per lane in the gel using ImageJ. Specifically, for each incubation point the intensity of the band corresponding to the full structure was divided by the intensity of this band at time zero to yield the relative percentage.

4.4. Cell culture

HeLa (cervical cancer) and MIA PaCa-2 (pancreatic cancer) cells were maintained in DMEM, supplemented with 10% fetal bovine serum (Thermo Scientific, Waltham, MA, USA) and 1% penicillin/streptomycin (Gibco). Cells were maintained at 37 °C with 5% CO_2 in a humidified incubator.

4.5. Flow cytometry

Atto488-labelled DNS were prepared for these studies. Cells were seeded on 96-well culture plates at a density of 5×10^5 cells per mL, cultured for 24 h and then washed twice with PBS. Then, they were incubated with fluorescently labelled DNS at a final concentration of 3 μM for the SST DNS and 7.5 μM for the Y-shaped DNS along with an equivalent concentration of S, at 37 °C for 3 h, harvested, and washed three times with 1× PBS. Subsequently, the geometric mean fluorescence intensity of the cells was determined by flow cytometry (CytoFLEX, Beckman Coulter, USA). Data were analysed using CytExpert and Kaluza software (versions 2.4 and 2.1 respectively; Beckman Coulter, USA). Fluorescence intensity is shown on a standard logarithmic scale.

4.6. Confocal microscopy

For confocal microscopy experiments, MIA PaCa-2 cells were seeded on glass coverslips in 24-well culture plates at a density of 10^5 cells per mL and incubated at 37 °C for 24 h. They were then washed twice with PBS and incubated with Atto488 labelled DNS at a final concentration of 3 μM in supplemented DMEM at 37 °C for 3 h. The medium was discarded, and cells were washed thrice with 1× PBS, followed by fixation using 4% paraformaldehyde for 15 min at room temperature (rt). The cells were again washed twice with 1× PBS. Afterwards, the cells were permeabilised with PBS-Saponin for 5 min and actin was stained with Alexa Fluor™ 546 phalloidin for 1 h at rt. Subsequently, the samples were washed with PBS-Saponin, followed by PBS and, finally, Milli-Q® water. In the last step, coverslips were mounted on the slide using Fluoromont-G (SouthernBiotech) which contains DAPI (Molecular Probes) to stain the cell nucleus. Cells were imaged using a Confocal Spectral Zeiss LSM 880 microscope (Leica TCS SP8) with a 63× oil immersion objective. Different fluorophores were excited

using three different lasers 405, 488 and 561 nm to visualise DAPI (cellular nucleus), Atto488 (labelled DNS) and AlexaFluor546 (actin), respectively. The image analysis was performed using the Zeiss Zen 3.4 software.

4.7. DOX encapsulation by fluorescence measurements

Fluorescence titration experiments were recorded at a constant drug concentration of 10 μM in PBS buffer and varying DNS bp concentrations from 0 to 65 μM. The fluorescence was measured using a fluorimeter (LS-55 PerkinElmer) with a quartz microcuvette. The excitation wavelength was set at 487 nm (maximum absorbance of DOX), and the emission spectrum was recorded in the range from 520 to 700 nm. Analysis of the titration curve was performed using OriginPro 2016 software. First variation of maximum fluorescence at 595 nm as a function of the pb/DOX ratio was plotted. Next, a polynomial fit was applied to the graph and the equation of the fitted graph was used to determine the pb/DOX needed to reach the lowest residual fluorescence in which all DOX has been trapped.

4.8. Isothermal calorimetry study

ITC was performed on an Auto-iTC200 (MicroCal, GE Healthcare) calorimeter. Either 0T or 6S DNS were loaded into the sample cell (400 μL) at a concentration of 105 μM bp in TNaK buffer (600 mM NaCl, 20 mM Tris-HCl and 5 mM KCl). DOX diluted in TNaK buffer was loaded into a 150 μL syringe. A total number of 19 injections (2 μL per injection) of the DOX solution were done every 150 s into the sample cell at 25 °C.

4.9. DOX release study

DOX release was monitored by fluorescence measurements using the same equipment and parameters as described in the DOX encapsulation section. Samples were incubated with different concentrations of DNase I or during different times in DMEM + FBS 10% previous fluorescence analysis. The percentage of release from the DNS was calculated by setting free DOX fluorescence at 10 μM as 100% release and residual DOX fluorescence as 0% release.

4.10. Cell viability study

The effect of DOX on cellular viability was investigated by measuring the activity of the mitochondrial dehydrogenase enzyme using the MTT assay. The HeLa and MIA PaCa-2 cells were seeded in 96-well plates at a density of 10 000 cells per well. After incubation for 24 h, the medium was eliminated and a new medium containing DOX, DNS and DOX-loaded DNS was added and incubated for 3 h at 37 °C. The DNS concentration to hold DOX was 40 ng μL^{-1}. Thereafter, the medium was discarded, and wells were washed once with PBS followed by new supplemented DMEM addition. After 24 h of incubation, the wells were washed once and the new supplemented medium without phenol red and with 5 mg mL^{-1} MTT solution was added to each well for 2 h. After that, the solution was removed, and subsequently, 100 μL of DMSO was added to each well. The plates were shaken for 5 min, and the absorbance was measured (540 nm) with a microplate reader (Multiskan GO, ThermoScientific). Viability of cells incubated with PBS instead of DNS/DOX was set as 100%.

4.11. Statistical analysis

Analyses were performed using GraphPad Prism (GraphPad). One-way ANOVA with the *post-hoc* test (Tukey test) was used on data with more than two groups. P values <0.05 were considered significant. $*p < 0.05$, $**p < 0.01$, $***p < 0.001$, $****p < 0.0001$, if not indicated: not significant.

Author contributions

The manuscript was written through the contribution of all authors. All authors have given approval to the final version of the manuscript.

Conflicts of interest

There are no conflicts to declare.

Acknowledgements

The authors acknowledge grant PID2020-113003GB-I00 funded by MCIN/AEI/10.13039/501100011033, and funds from the Research Group grant (E47_20R and E47_23R) by Gobierno de Aragón-FSE and from LMP128_21 grant by Gobierno de Aragón. J. D. B. acknowledges grant RYC-2015-18471, funded by MCIN/AEI /10.13039/501100011033 and by "European Social Fund Investing in Your Future"; and grant CTQ2017-84087-R supported by MCIN/AEI/10.13039/501100011033, and by "European Regional Development Fund a Way of Making Europe" by the European Union. P. M. V. acknowledges funding by the European Research Council (ERC) under the European Union's Horizon 2020 Research and Innovation Programme (Grant agreement No. 853468). K. N. B. acknowledges funding by the Swiss National Science Foundation (Grant number 209730). The authors would like to acknowledge the Servicio General de Apoyo a la Investigación-SAI (Universidad de Zaragoza), Servicios Cientifico-Técnicos of CEQMA (CSIC-Universidad de Zaragoza) and of CIBA (IACS-Universidad de Zaragoza) for their support. The authors would also like to acknowledge Dr Maria Moros for her support with flow cytometry and Dr Olga Abian and Dr María San Anselmo for the supply of cells and their advice on cell culture.

References

1 N. C. Seeman, *Nature*, 2003, **421**, 427–431.
2 Y. Yoon, C. Lee and S. J. Kim, *J. Korean Phys. Soc.*, 2021, **78**, 343–350.

3 F. Zhang, J. Nangreave, Y. Liu and H. Yan, *J. Am. Chem. Soc.*, 2014, **136**, 11198–11211.
4 A. Keller and V. Linko, *Angew. Chem., Int. Ed.*, 2020, **59**, 15818–15833.
5 J. Weiden and M. M. C. Bastings, *Curr. Opin. Colloid Interface Sci.*, 2021, **52**, 101411.
6 R. R. Du, E. Cedrone, A. Romanov, R. Falkovich, M. A. Dobrovolskaia and M. Bathe, *ACS Nano*, 2022, **16**, 20340–20352.
7 C. R. Lucas, P. D. Halley, A. A. Chowdury, B. K. Harrington, L. Beaver, R. Lapalombella, A. J. Johnson, E. K. Hertlein, M. A. Phelps, J. C. Byrd and C. E. Castro, *Small*, 2022, **18**, 2108063.
8 D. Jiang, Z. Ge, H.-J. Im, C. G. England, D. Ni, J. Hou, L. Zhang, C. J. Kutyreff, Y. Yan, Y. Liu, S. Y. Cho, J. W. Engle, J. Shi, P. Huang, C. Fan, H. Yan and W. Cai, *Nat. Biomed. Eng.*, 2018, **2**, 865–877.
9 T. Zhang, T. Tian, R. Zhou, S. Li, W. Ma, Y. Zhang, N. Liu, S. Shi, Q. Li, X. Xie, Y. Ge, M. Liu, Q. Zhang and S. Lin, *Nat. Protoc.*, 2020, **15**, 2728–2757.
10 S. Jiang, Z. Ge, S. Mou, H. Yan and C. Fan, *Chem*, 2021, **7**, 1156–1179.
11 B. R. Madhanagopal, S. Zhang, E. Demirel, H. Wady and A. R. Chandrasekaran, *Trends Biochem. Sci.*, 2018, **43**, 997–1013.
12 M. M. C. Bastings, F. M. Anastassacos, N. Ponnuswamy, F. G. Leifer, G. Cuneo, C. Lin, D. E. Ingber, J. H. Ryu and W. M. Shih, *Nano Lett.*, 2018, **18**, 3557–3564.
13 A. Rajwar, S. R. Shetty, P. Vaswani, V. Morya, A. Barai, S. Sen, M. Sonawane and D. Bhatia, *ACS Nano*, 2022, **16**, 10496–10508.
14 P. Wang, M. A. Rahman, Z. Zhao, K. Weiss, C. Zhang, Z. Chen, S. J. Hurwitz, Z. G. Chen, D. M. Shin and Y. Ke, *J. Am. Chem. Soc.*, 2018, **140**, 2478–2484.
15 B. Wei, M. Dai and P. Yin, *Nature*, 2012, **485**, 623–626.
16 K. Göpfrich, T. Zettl, A. E. C. Meijering, S. Hernández-Ainsa, S. Kocabey, T. Liedl and U. F. Keyser, *Nano Lett.*, 2015, **15**, 3134–3138.
17 J. Joseph, K. N. Baumann, A. Postigo, L. Bollepalli, S. E. Bohndiek and S. Hernández-Ainsa, *Adv. Healthcare Mater.*, 2021, **10**, 2001739.
18 J. B. Welch, D. R. Duckett and D. M. J. Lilley, *Nucleic Acids Res.*, 1993, **21**, 4548–4555.
19 M. Yang and D. P. Millar, *Biochemistry*, 1996, **35**, 7959–7967.
20 K. N. Baumann, L. Piantanida, J. García-Nafría, D. Sobota, K. Voïtchovsky, T. P. J. Knowles and S. Hernández-Ainsa, *ACS Nano*, 2020, **14**, 2316–2323.
21 B. Heddi, J. Abi-Ghanem, M. Lavigne and B. Hartmann, *J. Mol. Biol.*, 2010, **395**, 123–133.
22 C. E. Carr and L. A. Marky, *Biophys. J.*, 2018, **114**, 2764–2774.
23 D. S. Lee, H. Qian, C. Y. Tay and D. T. Leong, *Chem. Soc. Rev.*, 2016, **45**, 4199–4225.
24 M. M. Koga, A. Comberlato, H. J. Rodríguez-Franco and M. M. C. Bastings, *Biomacromolecules*, 2022, **23**, 2586–2594.
25 D. Mathur, A. R. Galvan, C. M. Green, K. Liu and I. L. Medintz, *Nanoscale*, 2023, **15**, 2516–2528.
26 J. Liu, M. Li and X. Zuo, *Small*, 2022, **18**, 2204711–2204711.
27 W. L. Whitehouse, J. E. Noble, M. G. Ryadnov and S. Howorka, *Bioconjugate Chem.*, 2019, **30**, 1836–1844.
28 O. Tacar, P. Sriamornsak and C. R. Dass, *J. Pharm. Pharmacol.*, 2013, **65**, 157–170.
29 H. Ijäs, B. Shen, A. Heuer-Jungemann, A. Keller, M. A. Kostiainen, T. Liedl, J. A. Ihalainen and V. Linko, *Nucleic Acids Res.*, 2021, **49**, 3048–3062.
30 I. Manet, F. Manoli, B. Zambelli, G. Andreano, A. Masi, L. Cellai and S. Monti, *Phys. Chem. Chem. Phys.*, 2011, **13**, 540–551.
31 Y. X. Zhao, A. Shaw, X. Zeng, E. Benson, A. M. Nyström and B. Högberg, *ACS Nano*, 2012, **6**, 8684–8691.
32 M. Chang, C. S. Yang and D. M. Huang, *ACS Nano*, 2011, **5**, 6156–6163.
33 Q. Jiang, C. Song, J. Nangreave, X. Liu, L. Lin, D. Qiu, Z. G. Wang, G. Zou, X. Liang, H. Yan and B. Ding, *J. Am. Chem. Soc.*, 2012, **134**, 13396–13403.
34 Q. Zhang, Q. Jiang, N. Li, L. Dai, Q. Liu, L. Song, J. Wang, Y. Li and J. Tian, *ACS Nano*, 2014, **22**, 6633–6643.
35 L. Li, S. Nie and J. Zhao, *MedComm*, 2023, **2**, e37.
36 A. Lacroix and H. F. Sleiman, *ACS Nano*, 2023, **15**, 3631–3645.
37 R. Veneziano, S. Ratanalert, K. Zhang, F. Zhang, H. Yan, W. Chiu and M. Bathe, *Science*, 2016, **352**, 1534.
38 J.-W. Keum and H. Bermudez, *Chem. Commun.*, 2009, 7036–7038.
39 A. S. Walsh, H. Yin, C. M. Erben, M. J. A. Wood and A. J. Turberfield, *ACS Nano*, 2011, **5**, 5427–5432.
40 S. Ramakrishnan, H. Ijäs, V. Linko and A. Keller, *Comput. Struct. Biotechnol. J.*, 2018, **16**, 342–349.
41 E. L. Coleridge and K. E. Dunn, *Biomed. Phys. Eng. Express*, 2020, **6**, 065030.
42 Q. Li, D. Zhao, X. Shao, S. Lin, X. Xie, M. Liu, W. Ma, S. Shi and Y. Lin, *ACS Appl. Mater. Interfaces*, 2017, **9**, 36695–36701.
43 H. Zhang, Y. Ma, Y. Xie, Y. An, Y. Huang, Z. Zhu and C. J. Yang, *Sci. Rep.*, 2015, **5**, 10099.
44 M. I. Setyawati, R. V. Kutty and D. T. Leong, *Small*, 2016, **12**, 5601–5611.